RESEARCH ARTICLE

Key Points:
- Global lunar map of zero-phase reflectance derived from LOLA 1064 nm data
- Permanently shadowed regions in the poles are anomalously bright
- Bright PSRs could be due to water frost and/or less effective space weathering

Correspondence to:
P. G. Lucey,
lucey@higp.hawaii.edu

The global albedo of the Moon at 1064 nm from LOLA

P. G. Lucey[1], G. A. Neumann[2], M. A. Riner[3], E. Mazarico[4], D. E. Smith[5], M. T. Zuber[5], D. A. Paige[6], D. B. Bussey[7], J. T. Cahill[7], A. McGovern[7], P. Isaacson[1], L. M. Corley[1], M. H. Torrence[4], H. J. Melosh[8], J. W. Head[9], and E. Song[1]

[1]Hawaii Institute of Geophysics and Planetology, University of Hawai'i at Mānoa, Honolulu, Hawaii, USA, [2]Jet Propulsion Laboratory, California Institute of Technology, Pasadena, California, USA, [3]Planetary Science Institute, Tucson, Arizona, USA, [4]NASA Goddard Space Flight Center, Greenbelt, Maryland, USA, [5]Department of Earth, Atmospheric, and Planetary Sciences, Massachusetts Institute of Technology, Cambridge, Massachusetts, USA, [6]Department of Earth and Space Sciences, University of California, Los Angeles, California, USA, [7]Applied Physics Laboratory, Johns Hopkins University, Baltimore, Maryland, USA, [8]Department of Earth, Atmospheric, and Planetary Sciences, Purdue University, West Lafayette, Indiana, USA, [9]Department of Geological Sciences, Brown University, Providence, Rhode Island, USA

Abstract The Lunar Orbiter Laser Altimeter (LOLA) measures the backscattered energy of the returning altimetric laser pulse at its wavelength of 1064 nm, and these data are used to map the reflectivity of the Moon at zero-phase angle with a photometrically uniform data set. Global maps have been produced at 4 pixels per degree (about 8 km at the equator) and 2 km resolution within 20° latitude of each pole. The zero-phase geometry is insensitive to lunar topography, so these data enable characterization of subtle variations in lunar albedo, even at high latitudes where such measurements are not possible with the Sun as the illumination source. The geometric albedo of the Moon at 1064 nm was estimated from these data with absolute calibration derived from the Kaguya Multiband Imager and extrapolated to visual wavelengths. The LOLA estimates are within 2σ of historical measurements of geometric albedo. No consistent latitude-dependent variations in reflectance are observed, suggesting that solar wind does not dominate space weathering processes that modify lunar reflectance. The average normal albedo of the Moon is found to be much higher than that of Mercury consistent with prior measurements, but the normal albedo of the lunar maria is similar to that of Mercury suggesting a similar abundance of space weathering products. Regions within permanent shadow in the polar regions are found to be more reflective than polar surfaces that are sometimes illuminated. Limiting analysis to data with slopes less than 10° eliminates variations in reflectance due to mass wasting and shows a similar increased reflectivity within permanent polar shadow. Steep slopes within permanent shadow are also more reflective than similar slopes that experience at least some illumination. Water frost and a reduction in effectiveness of space weathering are offered as possible explanations for the increased reflectivity of permanent shadow; porosity is largely ruled out as the sole explanation. The south polar crater Shackleton is found to be among the most reflective craters in its size range globally but is not the most reflective, so mass wasting cannot be ruled out as a cause for the crater's anomalous reflectance. Models of the abundance of ice needed to account for the reflectance anomaly range from 3 to 14% by weight or area depending on assumptions regarding the effects of porosity on reflectance and whether ice is present as patches or is well mixed in the regolith. If differences in nanophase iron abundances are responsible for the anomaly, the permanently shadowed regions have between 50 and 80% the abundance of nanophase iron in mature lunar soil.

1. Introduction

The Lunar Orbiter Laser Altimeter (LOLA) [*Smith et al.*, 2010b], an instrument aboard the Lunar Reconnaissance Orbiter (LRO) spacecraft, is principally a laser altimeter used for quantitative topography and related cartographic and geodetic applications. But in addition to measuring the range of the spacecraft to the lunar surface, LOLA measures the energy and width of the returned laser pulse reflected by the Moon [*Smith et al.*, 2010b], a method [*Sun et al.*, 2006] pioneered using data from the Mars Orbiter Laser Altimeter [*Smith*, 1999; *Smith et al.*, 2001; *Zuber et al.*, 1992]. LOLA samples the lunar surface with a five-spot laser pattern with 5 m individual footprints, and a 28 Hz laser pulse gives rise to a net 10–12 m sampling

of the lunar surface below the LRO ground track. Over many months of observations these longitudinal profiles have yielded a high density of lunar ranges globally, with accompanying measurements of lunar reflectance.

The physical quantity that LOLA reports is the normal albedo, which is the reflectance of a spatially resolved surface element observed where the angle between the illumination source, surface element, and detector is zero, relative to a Lambert surface viewed normally observed at the same geometry [*Hapke*, 1993]. In astronomical terms, this angle is termed the phase angle, and this viewing geometry is called zero phase. Normal albedo is a special case of the quantity *I/F*, defined as the ratio of the measured radiance *I* to the irradiance *F* of an ideal diffusive Lambert surface in vacuum with 100% reflectance under the same illumination, measured at zero phase. For a dark surface like the Moon, the normal albedo is not sensitive to the orientation of the observed surface facet, so the measurements are not influenced by the local topography of the surface [*Hapke*, 1993]. Viewed from the Earth, this geometry occurs at every full Moon, and under these conditions the rims and walls of lunar craters and other features are not apparent, so even subtle variations in the intrinsic lunar albedo can be discerned.

However, with passive imaging using the Sun as the light source, normal albedo can only be measured along an observer-Sun-Moon line, so at high latitudes normal albedo is observed at oblique angles that become more extreme as the poles are approached. Because of the rugged lunar topography, some portions of the poles are permanently obscured from this measurement. LOLA's unique contribution is that it carries its own light source and has measured the normal albedo for the entire lunar surface viewed normally below the LRO spacecraft, enabling unprecedented views of the lunar polar regions.

The lunar poles are extreme environments in the inner solar system. *Urey* [1952] noted that because of the very small tilt of the lunar rotation axis with respect to its path around the Sun, topographic depressions such as craters in the polar regions would be permanently shaded from the Sun, allowing them to achieve very low temperatures. Detailed models of lunar permanent shadow predicted temperatures to be a few tens of kelvins [*Watson et al.*, 1961; *Ingersoll et al.*, 1992; *Salvail and Fanale*, 1994; *Vasavada*, 1999], and the Diviner Lunar Radiometer Experiment has measured temperatures near 20 K in some of the shadowed regions [*Paige et al.*, 2010]. It was recognized in the first quantitative study by *Watson et al.* [1961] that these extremely low-temperature surfaces could act as cold traps for any volatiles that might be present in the lunar environment. *Arnold* [1979] calculated anticipated water ice abundances based on assumptions of the impact rate of comets on the Moon, and since then wet asteroids and in situ production of water by chemical interaction with solar wind hydrogen have been added to potential volatile sources [*Housley et al.*, 1973]. Direct detection of volatiles has been reported using radar [*Nozette et al.*, 1996] and orbital neutron spectroscopy [*Feldman et al.*, 2000; *Mitrofanov et al.*, 2010], and a detection of volatiles was reported by the LCROSS lunar impact experiment into a lunar cold trap featuring a prominent neutron anomaly interpreted to be a hydrogen high at this location [*Colaprete et al.*, 2010; *Gladstone et al.*, 2010].

The LOLA reflectance experiment was specifically designed to detect surface frost in regions of permanent shadow by measuring the albedo. *Zuber et al.* [2012] reported the first results from this experiment and showed that the interior of the south polar crater Shackleton was anomalously bright with respect to its surroundings; they suggested that a surface deposit of a few tens of percent water ice frost could account for this anomaly and also in the case of Shackleton that reduction in the effectiveness of space weathering due to its steep walls offering partial protection of the interior from micrometeorites was a preferred explanation.

In this study, we report the results of a study of the global LOLA reflectance data set, enabling direct comparison among lunar regions, including the polar regions. We present the unprecedented polar views and how the poles compare in reflectance to the Moon as a whole; an estimate of the 1064 nm geometric albedo of the Moon and its value over the entire surface and compare it to that of Mercury; and the reflectance properties of the regions of permanent shadow in the polar regions and constraints on the influence of lunar geologic properties on local brightness anomalies, including a closer look at Shackleton.

2. Calibration

In principle, laser reflectance measurements are straightforward. Given preflight calibrations of laser outgoing energy and receiver sensitivity, the reflectance of a surface is the ratio of the returned energy to the

transmitted energy, compensated for range. LOLA exhibited instrument anomalies [*Smith et al.*, 2010a] that caused sensitivity drifts with time over the course of the mission and strong variations along each orbit. These problems have been characterized with corrections applied to the data reported here and described in detail in the appendix. The consequence of these drifts is first that only a small portion of LOLA range measurements are suitable for reflectance measurements and that the absolute calibration of normal albedo is lost. The data reported here are calibrated to discrete measurements of normal albedo at several equatorial locations by the Kaguya Multiband Imager [*Kodama et al.*, 2010; *Ohtake et al.*, 2010], so our absolute values are entirely dependent on the quality of the calibration of that instrument (see appendix). However, LOLA's relative global measurements are internally consistent and not dependent on other measurements.

In addition to views of unilluminated portions of the lunar surface, these LOLA data also offer the advantage that no photometric normalization is required to compare measurements of different portions of the lunar surface because of the constant phase angle. As noted above, for the low-albedo Moon, zero-phase reflectance is not sensitive to the local slope [*Hapke*, 1993], amply demonstrated by the lack of limb darkening exhibited by the full Moon where incidence and emergence angles reach 90°.

3. Data

LOLA topography and reflectance data are obtained as profiles along the LRO orbit, so continuous images are produced by sampling the data set at the desired resolution and interpolating between the very narrow data strips. While the typical equatorial spacing of subsequent orbit tracks is about 20 km, by including several months with sufficient sensitivity to calibrate reflectance data, this spacing is substantially reduced and provides nearly continuous data at the equator when sampled at 4 pixels per degree of longitude and latitude (about 8 km spatial resolution). We then perform a simple linear interpolation along lines of latitude to fill in the data gaps. Data within 70° of latitude from the equator are sampled at this frequency.

At the poles the ground track sampling is much higher, and in this case the data are sampled at 2 km/pixel (the inherent resolution of the LOLA reflectance data set owing to the need for down track sampling, see appendix).

4. Results

Figure 1 shows orthographic projections of LOLA normal albedo data of four hemispheres of the Moon: the familiar Earth-facing view, a view centered on the lunar farside, and unprecedented views centered on the lunar north and south poles. The Earth-facing hemisphere appears extremely similar to an Earth-based full Moon photograph with the prominent dark maria apparent, as well as large, rayed craters. The albedo contrast within the maria is subtly different than views taken in visible light, exhibiting slightly more contrast among the different types of lunar maria owing to the position of the LOLA wavelength within the ferrous iron absorption band. Overall, this image obtained at zero-phase angle is familiar and new features have not been revealed in these data. To lunar experts, the farside view is also familiar, having been photographed by spacecraft since the 1960s. The farside exhibits much less exposure of lunar maria and dramatically exposes the low-albedo pattern associated with the vast South Pole-Aitken basin that dominates the southern farside hemisphere. This feature was first noted in data collected by the Galileo spacecraft en route to Jupiter in observations with a very low phase angle facilitating detection of subtle albedo features [*Head et al.*, 1993].

4.1. Variation in Albedo With Latitude

For the first time, the latitude-dependent albedo of the entire Moon can be characterized at a constant viewing geometry using these data. The reflectance of the Moon is strongly affected by the exposure of the lunar surface to the space environment in form of physical and chemical alterations by sputtering from the solar wind and micrometeorite impact. Among the many effects of this process known as *space weathering*, lunar soil is much darker than pulverized lunar rock of a similar composition [*Fischer and Pieters*, 1994]. Transmission electron microscopy has revealed that lunar soil grains are often coated with rims, consistent with vapor deposition from either sputtering or micrometeorite impact [*Keller and McKay*, 1993].

Figure 1. Four views of the normal albedo of the Moon at 1064 nm in orthographic projection: (top left) Earth-facing view, (top right) farside view, (bottom left) north pole view, and (bottom right) south pole view.

These rims are infused with extremely fine-grained (tens to hundreds of nanometer) iron spherules that are extremely efficient optical absorbers, and radiative transfer theory shows that lunar darkening is consistent with the presence of these spheres [*Hapke*, 2001]. Whether the vapor-deposited rims originate largely from sputtering or from micrometeorite impact is controversial, however, though recent work has suggested sputtering by the solar wind is the dominant cause [*Blewett et al.*, 2011].
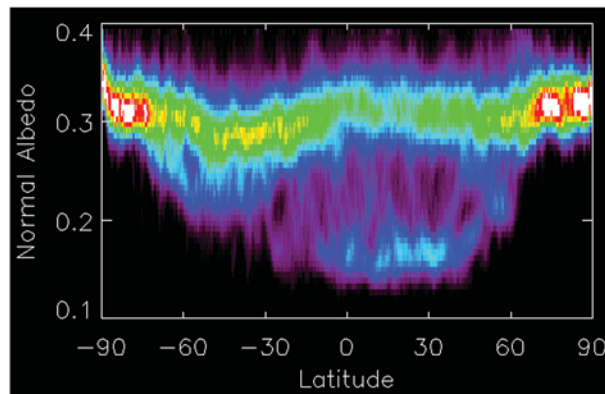

Figure 2. The distribution of normal albedo with latitude. Colors indicate the density of data points with warm colors being high density and cool colors low. White corresponds to the highest density of points.

LOLA reflectance data bear directly upon this issue. The solar wind illuminates the Moon very unevenly, with both a strong latitudinal gradient consistent with the solar source, and a longitudinal variation due to the Moon's passage through the Earth's magnetotail that partially shields portions of the Moon from the solar wind at times of the month [*Johnson et al.*, 1999]. If sputtering dominated lunar darkening, a latitude-dependent albedo would be the expected result. Previous measurements at or near-zero phase from the Earth and Galileo do not report a latitude dependence, but these measurements were not obtained at LOLA's constant geometry; both the solar incidence angle and emission angle of the
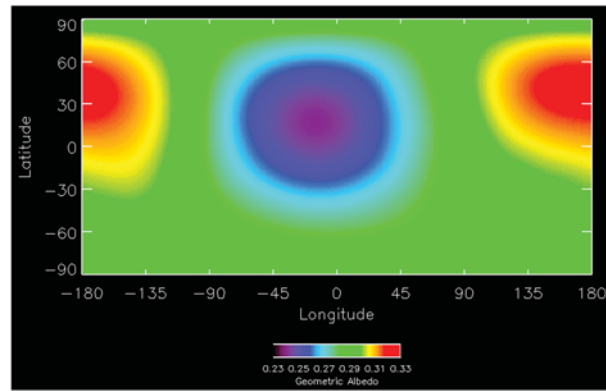
Figure 3. The geometric albedo of the Moon at 1064 nm as a function of central latitude and longitude.

lunar reflectance vary continuously in these measurements, possibly obscuring a latitudinal effect. Global reflectance measurements by passive sensors in lunar orbit have roughly uniform emergence angles, but solar incidence angles vary directly with latitude, so these measurements require correction for viewing angle effects. The corrections are in part empirical and so can introduce or normalize latitude (incidence) angle effects. LOLA measurements, featuring nearly constant phase angle and nadir view require none of these corrections.

Figure 2 shows the distribution of normal albedo with latitude. The bulk of the data are near a normal albedo of 0.3 corresponding to typical highlands material. A low-albedo mode occurs between 0 and 30° latitude with values near 0.15; these are the major deposits of lunar mare basalts. Between −90 and −20 latitude reflectance values are depressed due to the South Pole-Aitken albedo anomaly and Mare Smythii. The data do not show strong latitude dependence, though a slight uptick in reflectance is observed at both poles above 70° latitude. The LOLA data do not show a distribution of albedo that indicates dominance of space weathering by solar wind, in contrast to other evidence supporting the importance of solar wind [*Blewett et al.*, 2011].

4.2. The Geometric Albedo of the Moon at 1064 nm

Comparison of albedos among planets is facilitated by normalization to a common viewing geometry, and geometric albedo is typically exploited in this role. The geometric albedo is the integrated reflectance of a planetary object in orthographic projection, measured where the angle between the illumination, object, and observer—the phase angle—is zero, relative to a Lambert disk (ideal diffuse surface) also observed at zero-phase angle (the normal albedo). Integrating the normal albedo over the projected surface of an object yields the geometric albedo for a specific central latitude and longitude for objects lacking limb darkening like the Moon. Because of its special geometry, geometric albedo is a useful metric for comparing the surface reflectances of planets.

Warell [2004] presented his own and several prior estimates of the geometric albedo of the Moon at visual (V band) wavelengths [*Helfenstein and Veverka*, 1987; *Lane and Irvine*, 1973; *Lumme and Irvine*, 1982; *Shevchenko*, 1982] with values ranging from 0.113 to 0.163. To directly compare our results to the prior estimates, we take into account the fact that the Moon is spectrally red, that is, increases in reflectance with wavelength. We use data from Clementine [*Nozette et al.*, 1994], sampled at 4 pixels per degree to develop a correction and take the average of the 415 and 750 nm Clementine bands as a proxy for V band and the average of the 1000 and 1100 nm bands for the LOLA 1064 nm wavelength. We then ratio these proxy bands and multiply the ratio (0.583) by the LOLA normal albedo data to produce an estimated V band normal albedo. Finally, we project those data orthographically centered on 0,0 latitude and longitude and take the mean. The resulting estimate of V band geometric albedo from LOLA, Kaguya and Clementine is 0.169, just over the highest prior estimate for V band (0.162) and within 2σ of the *Warell* [2004] summary of
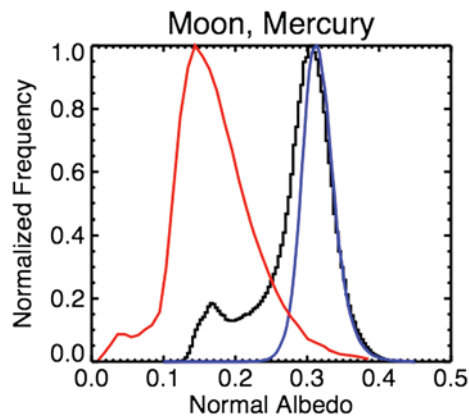

Figure 4. The normal albedos of the Moon (black), the lunar polar regions with 20° of the poles (blue), and the north polar region of Mercury (red). Mercury data from *Neumann et al.* [2013].
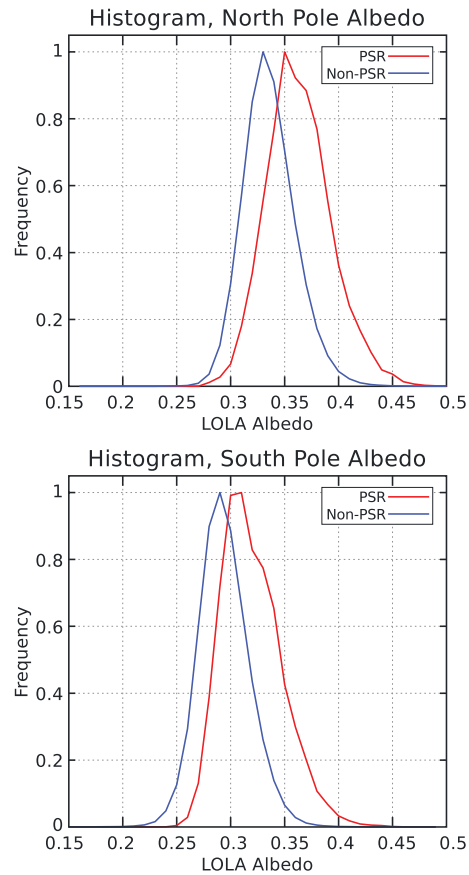
Figure 5. The distribution of normal albedo in regions of permanent shadow (red) and sometimes illuminated regions (blue) for latitudes within 20° of each pole. (top) North pole. (bottom) South pole.
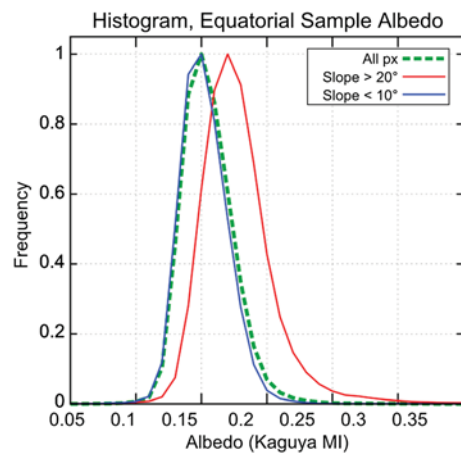

Figure 6. Histograms for an equatorial swath between 150 and 190° longitude and ± 15° of latitude. Reflectances of all points (green), surfaces with slopes greater than 20° (red), and slopes less than 10° (blue). Mass wasting has exposed less weathered surfaces on steep slopes, causing the reflectance of the distribution to shift to higher values by 0.02 units of reflectance. Albedo data from Kaguya Multiband Imager, slope data from LOLA.

estimates. Given the uncertainties associated with Clementine and Kaguya Multiband Imager calibrations [*Besse et al.*, 2013; *Hillier*, 1999; *Ohtake et al.*, 2010, 2013; *Pieters et al.*, 2013], our estimate of geometric albedo is consistent with prior work.

The geometric albedo of the Moon at 1064 nm as viewed from any direction can be derived from these data. For a particular central latitude and longitude, we resample the data using orthographic projection and report the mean albedo of the projection. Figure 3 shows the geometric albedo as a function of central latitude and longitude at 1° increments, varying from a high of 0.33 centered on the northern lunar farside, to a low of 0.24 centered nearly on the region that faces the Earth. These direct measurements of geometric albedo for all aspects of a single object are unique and can be used to compare estimated geometric albedos for other objects. For example, studies of exoplanets that eventually derive albedos can use these results to constrain the interpretation of these results [e.g., *Sudarsky et al.*, 2000].

These new data can be directly compared to recent observations of Mercury by the MErcury Laser Altimeter on the MErcury Surface, Space ENvironment, GEochemistry, and Ranging (MESSENGER) spacecraft [*Neumann et al.*, 2013]. A variety of experiments suggest that Mercury is darker than the Moon [e.g., *Denevi and Robinson*, 2008]; the LOLA data allow comparison at the unique zero-phase geometry. We find that the normal albedo of Mercury's north polar region is much lower than the lunar highlands and similar to that of the lunar maria (Figure 4). The albedo of the Moon is dominated by the space weathering product nanophase iron, produced during micrometeorite impact and by sputtering, so these results suggest that the surface of Mercury may contain amounts of nanophase absorbers similar to that of the lunar maria, despite the low iron of the background material.

4.3. The Reflectance Properties of Permanently Shadowed Regions

One of LOLA's goals is the search for possible surface frost in the lunar polar regions based on detection of reflectance anomalies [*Smith et al.*, 2010b]. As outlined in section 1, *Zuber et al.* [2012] found that the floor of the south polar crater Shackleton was indeed anomalously bright with respect to its immediate south polar surroundings, consistent with a 1 μm surface layer with ~20% surface frost, but cautioned that mass wasting, common on the Moon within steep-walled craters, was a likely explanation for the local enhancement. Using LOLA global reflectance measurements, we can test whether regions of permanent shadow are, in general, anomalous relative to areas that are sometimes illuminated.
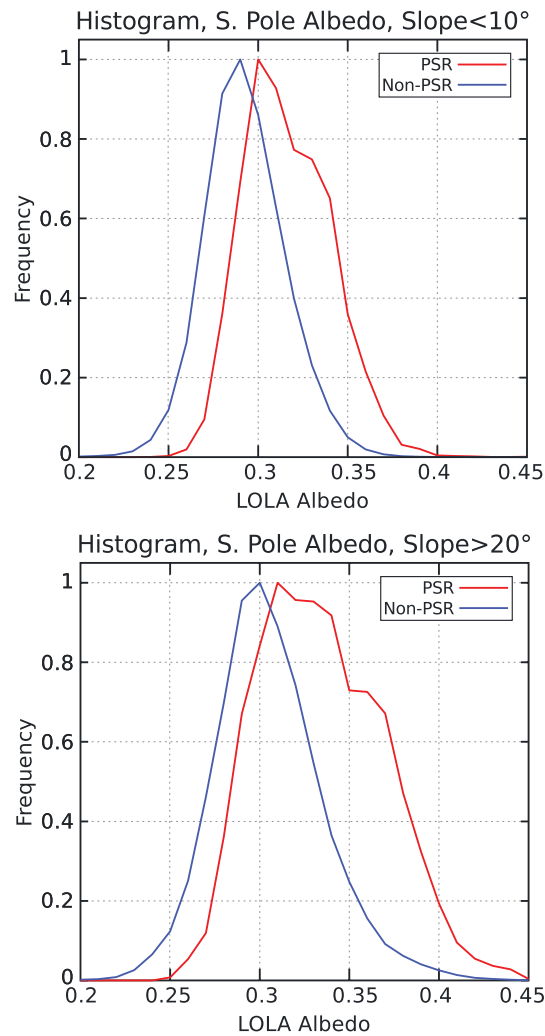
Figure 7. Distribution of LOLA normal albedo in the south polar region within (red) and outside (blue) of PSRs. (top) Surfaces with slopes less than 10°. (bottom) Surfaces with slopes greater than 20°.

McGovern et al. [2013] calculated maps of degree of illumination in the current era, including areas that never receive direct sunlight, and we use their data to create masks of the location of regions of permanent shadow. Figure 5 gives the distributions of LOLA normal albedo within permanently shadowed regions (PSRs) and regions that are sometimes illuminated (non-PSRs). There is a significant offset in the distributions of reflectance between PSR and non-PSR, though the distributions show significant overlap (meaning some areas of permanent shade exhibit lower reflectance than some areas that receive illumination). Because shaded regions are frequently associated with steep, pole-facing slopes, we reiterate the caution offered by *Zuber et al.* [2012] that normal lunar geologic processes, specifically mass wasting, can cause the lunar surface to have higher reflectance locally. Mass wasting—the downslope movement of unconsolidated debris—causes local increases in reflectance because it exposes material that has been not previously been subject to the darkening effect of space weathering. To more accurately compare the reflectance of PSR and non-PSR, we must control for slope to mitigate the possibility that the topography that gives rise to PSRs may allow mass wasting to cause the PSR average brightness to be greater than areas that receive illumination.

We examine the effect of slope on reflectance both in the equatorial region lacking any permanent shadow and possibility of surface frost, and in the polar regions. Using the LOLA digital elevation model sampled at 240 m/pixel [*Smith et al.*, 2010a], we derive local slope and aspect for each pixel by fitting a plane to the eight neighboring pixels. We defined a control area at the equator bounded between 150 and 190° longitude and ± 15° of latitude, approximately the same total area as the polar regions above 70° latitude. LOLA reflectance data are sampled coarsely in the equatorial region, so for this analysis we use data from the Kaguya Multiband Imager that has been corrected for topographic shading. In this equatorial region, the reflectance of surfaces with slopes less than 10° is significantly lower than those with slopes greater than 20°, which we interpret to plausibly demonstrate the effect of mass wasting. In this large equatorial region, the slope-dependent shift in the reflectance distribution is 0.02 (Figure 6).

Applying this lesson, we compare the reflectance of surfaces within and outside regions of permanent shadow with slopes less than 10° where mass wasting is ineffective. A substantial difference in reflectance between PSR and non-PSR still persists; even flat-lying regions in permanent shadow typically have higher albedos than flat-lying regions sometimes illuminated (Figure 7), with the shift in the distribution of about 0.03. We also observe that steeply sloped areas within permanent shadow also have higher reflectances than regions outside permanent shadow with the same range of steep slopes, also with a shift of the mean of about 0.03 in reflectance (Figure 7). These results show that mass
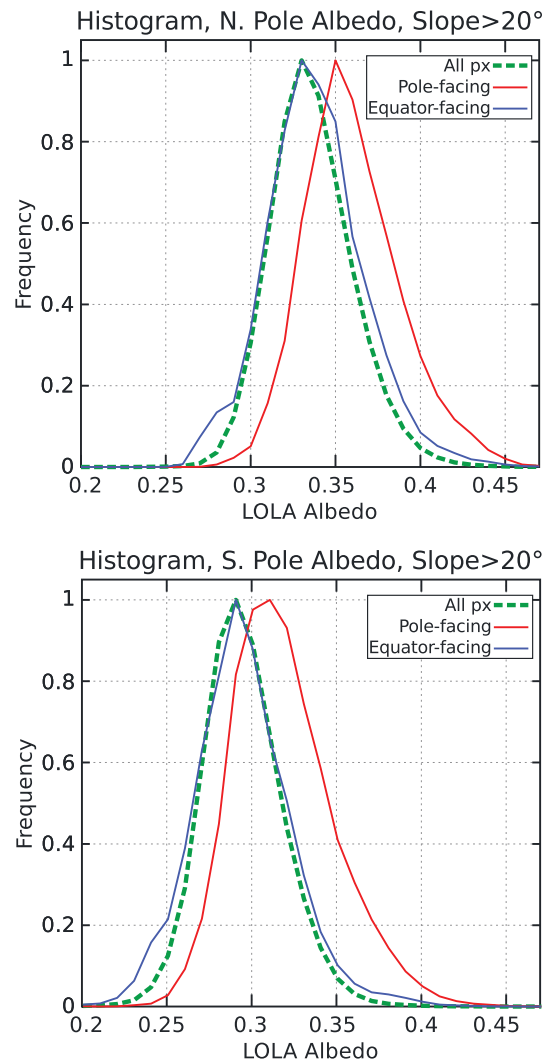
Figure 8. Distribution of LOLA normal albedo in the south polar region with slopes greater than 20°, pole-facing surfaces (within 45° of azimuth) (red), and equator-facing surfaces (blue). (top) North Pole. (bottom) South Pole.

wasting cannot account for the systematic difference between regions of permanent shadow and areas that are sometimes illuminated, providing that mass wasting itself is not influenced by properties within the permanently shadowed regions.

A second potential property that could account for the systematic difference between PSRs and areas sometimes illuminated is the degree to which these surfaces are exposed to space, a parameter we call sky access. Topographic variations will cause variations in the solid angle of space to which a surface is exposed. The bottom of a steep-walled crater will be partly shielded by the walls of the crater, while the top of a mountain may view more than a hemisphere. While neither micrometeorite flux nor solar wind is expected to be an isotropic source, the geometric extent of the exposed sky will tend to influence the intensity of these sources and so the local intensity of space weathering. By ray tracing, we determined the sky exposure for each polar pixel within 20° of each pole. In the north polar region, regions with limited sky access (defined as < 4.5 sr) are, in general, brighter than regions with more sky access (5–6 sr) (Figure 9), consistent with a space weathering control on reflectance. Sky view is somewhat correlated with slope because pixels on steep slopes tend to have more limited sky views, so this result can be confused with a control by mass wasting.

To further test the notion that the PSRs are intrinsically brighter than non-PSR surfaces, we confine comparison to similar sky views. When we control the comparison of PSR and non-PSR to similar sky views, we find again that the PSRs are consistently brighter than the non-PSRs even

when sky view is held constant; that is, areas in PSRs with a given sky view are brighter than illuminated surfaces with similar sky views. This suggests that differences in intensity of the space weathering sources (sputtering and micrometeorites) imposed by sky access do not explain the difference between PSRs and areas that are sometimes illuminated.

These results lead to the conclusion that the environment within the PSRs, not their geometry or geologic setting, is controlling their enhanced reflectance at 1064 nm.

4.4. Models of 1064 nm Polar Reflectance

Three hypotheses have been presented to explain polar surface reflectance anomalies. *Zuber et al.* [2012] suggested the presence of surface frost, as noted. *Gladstone et al.* [2012] showed that permanent shadow was systematically darker in UV reflectance measurements of the polar regions obtained with the Lunar Atmosphere Mapping Project (LAMP) UV spectrometer at 122 nm. They suggested that substantially higher porosity in the PSRs could account for their UV properties, perhaps caused by a difference in electrostatic forces in the cold traps enhancing the notable fairy castle structure of lunar soil. Finally, *Zuber et al.* [2012] suggested that the difference may be caused by an environmental
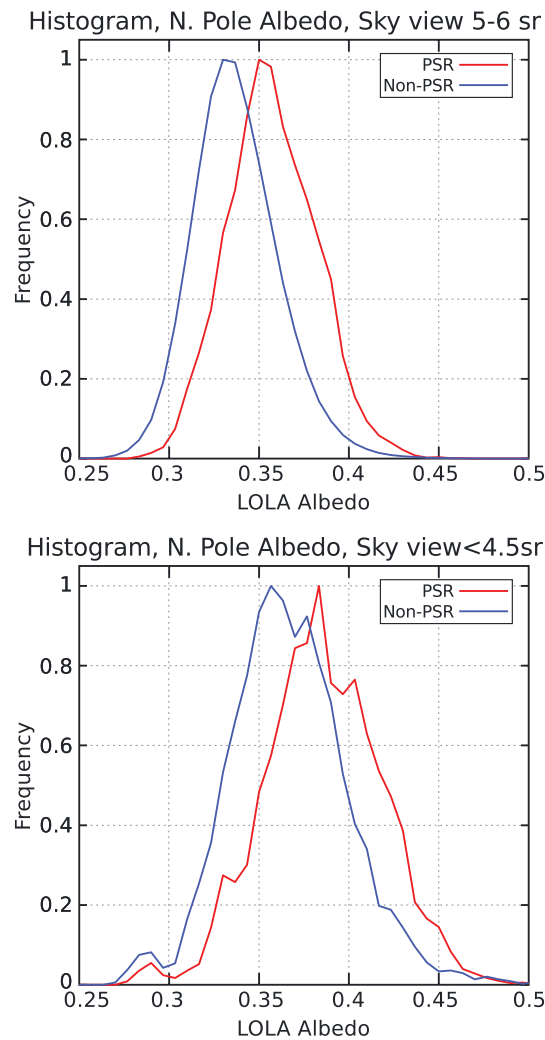
Figure 9. Distribution of LOLA normal albedo with sky view for the north polar region. (top) Sky access 5–6 sr for permanent shadow (red) and illuminated (blue). (bottom) Areas with limited sky view (<4.5 sr), for permanent shadow (red) and illuminated (blue).

influence on the effectiveness or rate of space weathering within the permanently shadowed regions. We will examine the consistency of these hypotheses with LOLA reflectance data.

The Lunar Atmosphere Mapping Project (LAMP) produced maps of the UV reflectance of the polar regions using reflected starlight and Lyman alpha emission scattered off interplanetary hydrogen [*Gladstone et al.*, 2012]. The results show that the UV reflectance of the PSRs is strikingly lower than the areas sometimes illuminated (Figure 10) They noted that porosity has a strong effect on reflectance and used quantitative models to show that a change in porosity from about 0.4 to 0.7 could account for the UV reflectance difference, and hypothesized that the polar environment may encourage higher porosity though increased electrostatic forces.

To test if porosity could account for the LOLA results, we model the porosity effect on near-infrared (NIR) reflectance. *Hapke* [2008] presented methods to estimate the effect of porosity both on plane albedo, the quantity measured by LAMP, and bidirectional reflectance, the quantity measured by LOLA (of which normal albedo is a special case). *Hapke* [2008] cautioned that his treatment was only valid over a defined range of porosities for a given wavelength. At 1064 nm and for the most optically active size range of lunar soil, 10–20 µm, Hapke's work is valid for porosities above about 0.5, conveniently overlapping most measured lunar porosities. We then use Hapke's treatment to calculate the reflectance of the PSRs assuming the porosity proposed by *Gladstone et al.* [2012].

We start with the typical reflectance of the illuminated surface as the mode of the histogram of the illuminated portion (0.33, Figure 4). We then estimate the single-scattering albedo of the illuminated surface using a reflectance value of 0.33 at the zero-phase condition [*Hapke*, 2008, equation 31] and assuming a porosity of 0.5 [*Carrier et al.*, 1991]. That derived single-scattering albedo is 0.61. We then compute the reflectance at zero phase for a surface with that single-scattering albedo and a porosity of 0.7, with a result of 0.26. This value is, as expected, lower than the reflectance of the starting materials in the sometimes illuminated region and much lower than the observed reflectance in PSRs (mode of the distribution = 0.36). This shows that porosity *alone* cannot account for both the LOLA and LAMP results. However, below we will include porosity in determining if frost is consistent with measurements.

Surface frost remains a viable hypothesis in light of this more extensive LOLA analysis. As modeled by *Zuber et al.* [2012], a thin layer of water ice frost could account for the Shackleton anomaly, and by extension the rest of the poles. However, while the mean reflectance of the PSR is higher than the mean reflectance outside PSR, not all PSR surfaces are anomalously bright, so if frost is present, it is not
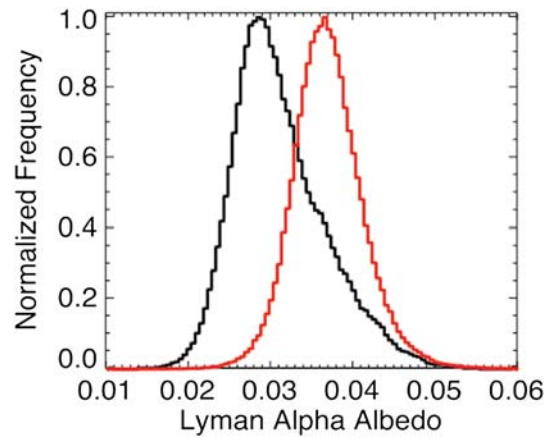
Figure 10. Histograms of Lyman α albedo for the south polar region. Red represents areas that are sometimes illuminated; black represents areas in permanent shadow. Permanent shadow is generally darker than areas that receive illumination, but substantial overlap is present between the two illumination conditions.

uniformly distributed. Similarly, the LAMP UV measurements of the spectral slope in the UV that is sensitive to water frost (as opposed to the general UV darkening) is also variable in the PSR [*Gladstone et al.*, 2012]. Nevertheless, we can calculate the average frost abundance that can account for the reflectance of the PSRs.

We look at four cases. We treat both linear mixing where frost patches might be present at the subpixel level and intimate mixing where frost grains are thoroughly mixed into the regolith. We consider these two models both including the porosity proposed by *Gladstone et al.* [2012] and neglecting porosity. Table 1 summarizes the inputs to the model.

We first treat the linear mixing case that governs frost distributed in discrete patches. This is the simple adding of the reflectances of the end-members weighted by their relative areas. For the dry end-member we use the reflectance of 0.33 as above. This value is used in the case where porosity is neglected. In the case where porosity is included we use the reflectance 0.26. For the ice end-member we take the absolute most conservative case of a normal albedo of 1.4, the albedo of Enceladus [*Verbiscer et al.*, 2006]. Solving for the frost fraction in both cases we get 3% frost coverage in the case where porosity is neglected, and 9% coverage where porosity is included (Table 2).

The intimate mixing case uses a nonlinear mixing systematic, which is linearized by mixing single-scattering albedos. For the ice end-member we use the optical constants of *Warren and Brandt* [2008] and the methods of *Hapke* [1993, 2008] to compute the single-scattering albedo. Regardless of porosity and even a large range of grain size, the single-scattering albedo of water ice at 1064 nm is close to 1, so for all cases we set it equal to 1.0. With porosity considered, the single-scattering albedo used for the silicate fraction is 0.61 (above and Table 1) and the single-scattering albedo of the shadowed surface is 0.74. In this case the ice abundance needed to match the shadowed surface single-scattering albedo is 14 wt %. With porosity neglected, the methods of *Hapke* [2008] are not used, and higher single-scattering albedos are derived, with 0.8 for the dry illuminated soil and 0.83 for the shadowed surface. In this case the ice fraction is 6 wt %. The results are summarized in Table 2.

4.5. Space Weathering

Space weathering has a profound influence on the reflectance of the Moon [*Fischer and Pieters*, 1994], and while we have eliminated systematic variations in the intensity of the space weathering source in accounting for the differences between PSR and non-PSR surfaces, this does not address any influence of the environment on the space weathering process itself. A plausible alternative to frost increasing the

Table 1. Reflectance and Single-Scattering Albedo Inputs to Mixing Model

	Porosity Neglected	Porosity Neglected	Porosity Considered	Porosity Considered
	Reflectance	Single-Scattering Albedo	Reflectance	Single-Scattering Albedo
Dry soil	0.33	0.80	0.26 (in shadow)[a]	0.61[b]
Shaded surface	0.36	0.83	0.36	0.74[c]
Ice	1.4	1.0	1.4	1.0

[a]Computed from $w = 0.61$, porosity = 0.7.
[b]Computed from $R = 0.33$, porosity = 0.5.
[c]Computed from $R = 0.36$, porosity = 0.7.

Table 2. Mixing Model Results

Mixture	Porosity Considered?	Ice Area Fraction	Ice Weight Fraction[a]
Linear	N	0.03	--
Linear	Y	0.09	--
Intimate	N	--	0.06
Intimate	Y	--	0.14

[a]Volume fraction computed from single-scattering albedos; the weight fraction computed assuming lunar soil has a grain density of 2.9 (90 anorthite, 2.8 g/cm^3; 10% orthopyroxene, 3.4 g/cm^3).

NIR reflectance is a reduction in the efficiency of space weathering leading to a deficit in the optical components that lead to darkening. The darkening effect of space weathering is due to extremely small spherules of iron produced as lunar soil matures. These spherules are present in vapor-deposited coatings on mineral grains from solar wind sputtering and micrometeorite impact vaporization, and in blebs of glass from micrometeorite impact melting [*Keller and McKay*, 1993, 1997]. The spheres in the coatings are typically very small, on the order of 10 nm, while the spheres in agglutinate glass are larger, up to several hundred nanometers [*Keller and Clemett*, 2001]. The optical effects of these spheres are well understood, and quantitative models are available [*Hapke*, 2001; *Lucey and Riner*, 2011]. We can use these models to estimate how much of this submicroscopic iron (SMFe) is present in the polar regions compared to the illuminated portions of the Moon.

As a quantitative starting point, we begin with the mature soil 62231 collect at the Apollo 16 site. This soil shows evidence of long space exposure with abundant submicroscopic iron totaling about 0.58 wt % [*Morris*, 1980]. The reflectance of this soil at 1064 nm can be modeled with a mixture of 85% plagioclase and 15% orthopyroxene by weight and 0.6 wt % submicroscopic iron. The optical effects of submicroscopic iron are strongly bimodal, with very small sizes (<30 nm) causing reddening and darkening, and larger sizes (>30 nm) causing darkening alone. In the model, we partition the submicroscopic iron according the measured difference in this lunar soil, with 0.1 wt % assigned to the small size fraction and 0.5 wt % assigned to the large fraction. Applying this model to the zero-phase condition (incidence and emission = 0) we adjust the intensity of the backscatter peak parameter, so the model soil normal albedo equals 0.33. We then adjust the amount of submicroscopic iron to match the normal albedo of the permanent shade of 0.36. We treated two cases, both including, and neglecting, the effects of porosity. Summarized in Table 3, neglecting porosity, the permanent shadow surface submicroscopic iron content is 0.8 times the illuminated surface. Including darkening effect of increased porosity, the submicroscopic iron content is half that of the illuminated surface.

4.6. The Reflectance Properties of Shackleton Crater

The report by *Zuber et al.* [2012] was the first use of LOLA reflectance data, and they noted that the floor of the south polar crater Shackleton, whose rim lies on the lunar south pole, displayed anomalously high reflectance with regard to the surrounding south polar region. The locally high reflectance was consistent with an exposure of surficial frost, but mass wasting of the crater walls and a possible dearth of space weathering were also noted to conceivably explain the observations. The global data of the current study allow the local observations from Shackleton to be placed in context with other geographically distributed craters of its size. We compared the albedos of the floor of Shackleton to those of 175 craters between 20 and 30 km in diameters situated between ±50° latitude. The craters were

Table 3. Space Weathering Product Abundances

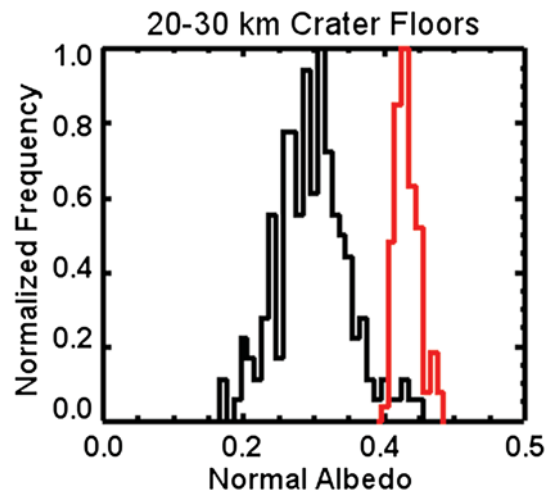|	Nanophase Iron ($<< \lambda$) wt %	Britt Pieters Particles (1 μm) wt %	Total SMFe	Ratio SMFe in PSR to Illuminated
Soil 62231	0.16 (FeOA)	0.42 (FeOC-FeOA)	0.58	-
Model Soil	0.1	0.5	0.6	-
Model PSR without porosity	0.08	0.42	0.5	0.8
Model PSR porosity = 0.7	0.05	0.26	0.31	0.5

Figure 11. Normal albedo of Shackleton floor (red) and the median normal albedo of the floors of similarly preserved 20–30 km diameter craters (black).

selected from the LOLA Large Crater Catalog of *Head et al.* [2010] and *Kadish et al.* [2011]. In order to select a population similar to Shackleton, the analysis was confined to those craters that displayed measurable reflectance anomalies on their walls, presumably due to mass wasting. The reflectance of the floor of Shackleton is anomalous, but not uniquely so. Figure 11 shows the distribution of average reflectances for the floors 20–30 km diameter craters; Shackleton's floor is among the highest reflectances. Complicating this analysis is the presence of anorthosite on the upper rim of Shackleton [*Haruyama et al.*, 2013], an extremely reflective material that could raise the albedo of the floor if transported that distance. *Zuber et al.* [2012] noted that Shackleton's steep walls could promote mass wasting, suggesting that more than one mechanism (for example, mass wasting and water frost) could be contributing to the relative brightening. LOLA measurements by themselves cannot definitively determine if Shackleton features anomalously high reflectance because of the unique average properties of permanent shadow, or if Shackleton is similar to the few extreme members of the equatorial craters of its size that share its high reflectance. Its reflectance is typical of regions of permanent shadow with steep slopes, and we judge it more likely to be a member of that class.

5. Discussion

The combination of the LAMP and LOLA results is a powerful constraint on the properties of the permanently shadowed regions. The two mechanisms for the increased reflectance at 1064 nm, frost and inhibited space weathering, are not very effective at darkening at 122 nm. The high absorbance of silicates and ice at these wavelengths does not promote the kind of high contrast observed, and while there are indications that space weathering causes some albedo changes [*Hendrix and Vilas*, 2006; *Hendrix et al.*, 2012, Figure 5], these do not appear to be sufficient to account for the observed anomalies within PSRs. Porosity remains the most viable mechanism for the UV darkening within the PSRs. However, this larger porosity implies that the frost or space weathering effects must overcome substantially lower background reflectance to achieve the observed increase in reflectance, leading to relatively high model abundances of frost, or low model abundances of submicroscopic iron. Whether the model abundances of submicroscopic iron in the PSRs are consistent with the UV data is not known owing to the lack of a validated quantitative model of their effects at these wavelengths, but the estimated frost abundances are high relative to the abundances estimated from the UV ice ratio [*Gladstone et al.*, 2012].

These models do make strong predictions regarding NIR reflectance properties of the polar regions. We modeled the spectral effect of the lower of the abundances (from the no-porosity areal and intimate mixture models) shown in Figure 12. In the case of areal mixtures, 3 wt % produces relatively strong bands at 1.5 and 2.0 μm. The band at 3 μm is a combination of the absorption due to ice and the intrinsic 3 μm band observed by Cassini, Deep Impact, and Chandrayaan-1 [*Clark*, 2009; *Pieters et al.*, 2009; *Sunshine et al.*, 2009]. In the intimate mixture the shorter wavelength bands are weaker, but the 3 μm band is greatly enhanced owing to the nonlinear nature of the mixing model. We also show the effect of 1 wt % water ice (by area and weight) with similar results. This suggests that spectral measurements could detect water ice in permanent shadow, for example, using scattered moonlight from crater walls, or using active illumination such as LOLA but at appropriate wavelengths. A failure to detect these enhanced water features would indicate ice is not present at the 1% level.
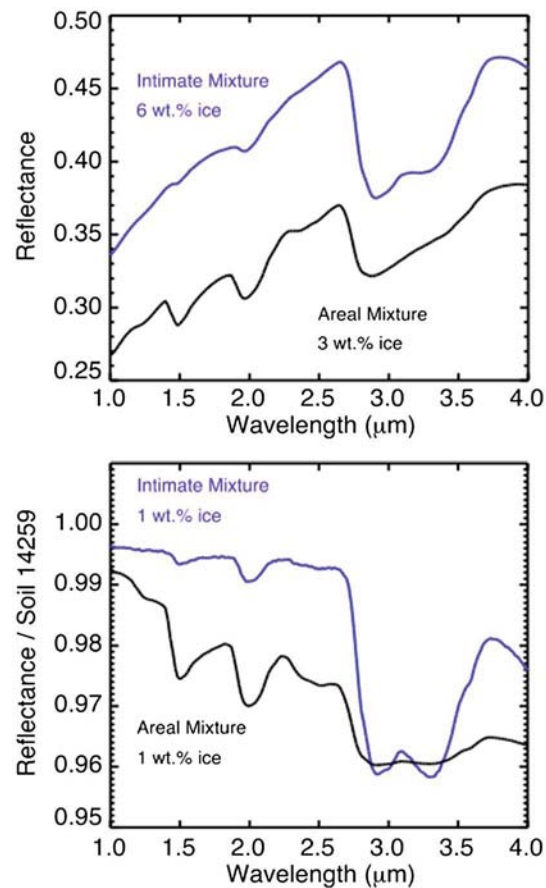
Figure 12. (top) Model spectra of water ice and lunar soil using ice abundances listed in Table 2. The intimate mixture is a weighted average of the single-scattering albedo spectrum of water frost with 10 μm size computed using the methods of *Hapke* [1993], converted to reflectance. The areal mixture spectrum uses the same end-members, weighted by the fractional area abundance. In the intimate case the overtone bands near 1.5 and 2.0 μm are relatively weak, but discernable, but the 3 μm feature is more intense. In the areal (patchy) mixture the overtone bands are relatively strong with less effect on the 3 μm band depth. (bottom) Spectra of 1% mixtures by weight and area, normalized to the spectrum of the dry lunar soil. At this abundance level the overtone bands show ~ 1% band depth in the areal case but are very weak in the intimate case. In contrast, at 3 μm the intimate mixture spectrum shows a very strong band.

Finally, the PSR property that almost certainly provides the conditions for the enhanced reflectance is the low maximum and average temperatures. These promote accumulation of frost if a source is present, for example, water produced from reduction of lunar oxygen by the solar wind, or may inhibit the formation of submicroscopic iron by reducing melting or vaporization by micrometeorites or effectiveness of sputtering. Detailed analysis of the temperature-reflectance relationships may shed further light on the permanently shadowed regions.

6. Conclusions

The LOLA reflectance experiment has produced a global nadir-viewing normal albedo data set for the Moon. Estimates of geometric albedo extrapolated to visible wavelengths are consistent with previous visual values within 2σ. Despite strong gradients in solar wind intensity with latitude, LOLA data show no obvious dependence of normal albedo upon latitude. These characteristics do not support sputtering as the dominant force driving space weathering.

The normal albedo of the Moon is generally much higher than that of Mercury, but the normal albedo of the lunar maria is similar to that of Mercury suggesting similar quantities of space weathering products.

The permanently shadowed regions are distinct in optical properties even when geologic conditions (slope, exposure to space) are controlled, suggesting an environmental control on these properties. The differences persist when comparisons are confined to steep or to shallow slopes or regions with large exposure or small exposure to space. Porosity alone cannot account for the NIR and UV differences between PSRs and areas sometimes illuminated but may be required to account for the UV properties. The presence of frost or a reduced amount of submicroscopic iron can both overcome the darkening due to porosity at 1064 nm, though required frost abundances are high relative to estimates derived from the UV. These results apply to the polar regions generally, but in the specific case of the crater Shackleton, the presence of anorthosite in the rim complicates interpretation. Frost at the 1% level should be readily detectable using spectroscopy in the NIR sensitive to the ice bands at 3 μm, and one of the 1.5 or 2 μm bands, making this a sensitive test of the frost hypothesis.

References

Arnold, J. R. (1979), Ice in the lunar polar regions, *J. Geophys. Res.*, *84*(B10), 5659–5668, doi:10.1029/JB084iB10p05659.

Besse, S., et al. (2013), One Moon, many measurements 2: Photometric corrections, *Icarus, 226*(1), 127–139, doi:10.1016/j.icarus.2013.05.009.

Blewett, D. T., E. I. Coman, B. R. Hawke, J. J. Gillis-Davis, M. E. Purucker, and C. G. Hughes (2011), Lunar swirls: Examining crustal magnetic anomalies and space weathering trends, *J. Geophys. Res.*, *116*, E02002, doi:10.1029/2010JE003656.

Carrier, W. D., G. R. Olhoeft, and W. Mendell (1991), Physical properties of the lunar surface, in *Lunar Sourcebook: A User's Guide to the Moon*, pp. 475–594, Cambridge Univ. Press, Cambridge.

Clark, R. N. (2009), Detection of adsorbed water and hydroxyl on the Moon with Cassini VIMS, Am. Astron. Soc.

Colaprete, A., et al. (2010), Detection of water in the LCROSS ejecta plume, *Science, 330*(6003), 463–8, doi:10.1126/science.1186986.

Denevi, B. W., and M. S. Robinson (2008), Mercury's albedo from Mariner 10: Implications for the presence of ferrous iron, *Icarus, 197*(1), 239–246, doi:10.1016/j.icarus.2008.04.021.

Feldman, W. C., D. J. Lawrence, R. C. Elphic, B. L. Barraclough, S. Maurice, I. Genetay, and A. B. Binder (2000), Polar hydrogen deposits on the Moon, *J. Geophys. Res.*, *105*(E2), 4175–4195, doi:10.1029/1999JE001129.

Fischer, E. M., and C. M. Pieters (1994), Remote determination of exposure degree and iron concentration of lunar soils using VIS-NIR spectroscopic methods, *Icarus, 111*(2), 475–488, doi:10.1006/icar.1994.1158.

Gladstone, G. R., et al. (2010), LRO-LAMP observations of the LCROSS impact plume, *Science, 330*(6003), 472–6, doi:10.1126/science.1186474.

Gladstone, G. R., et al. (2012), Far-ultraviolet reflectance properties of the Moon's permanently shadowed regions, *J. Geophys. Res.*, *117*, E00H04, doi:10.1029/2011JE003913.

Hapke, B. (1993), *Theory of Reflectance and Emittance Spectroscopy*, 1st ed., Cambridge Univ. Press, Cambridge, U. K.

Hapke, B. (2001), Space weathering from Mercury to the asteroid belt, *J. Geophys. Res.*, *106*(E5), 10,039–10,073, doi:10.1029/2000JE001338.

Hapke, B. (2008), Bidirectional reflectance spectroscopy, *Icarus, 195*(2), 918–926, doi:10.1016/j.icarus.2008.01.003.

Haruyama, J., S. Yamamoto, Y. Yokota, M. Ohtake, and T. Matsunaga (2013), An explanation of bright areas inside Shackleton Crater at the Lunar South Pole other than water-ice deposits, *Geophys. Res. Lett.*, *40*, 3814–3818, doi:10.1002/grl.50753.

Head, J. W., S. Murchie, J. F. Mustard, C. M. Pieters, G. Neukum, A. McEwen, R. Greeley, E. Nagel, and M. J. S. Belton (1993), Lunar impact basins: New data for the western limb and far side (Orientale and South Pole-Aitken Basins) from the first Galileo flyby, *J. Geophys. Res.*, *98*(E9), 17,149–17,181, doi:10.1029/93JE01278.

Head, J. W., C. I. Fassett, S. J. Kadish, D. E. Smith, M. T. Zuber, G. A. Neumann, and E. Mazarico (2010), Global distribution of large lunar craters: Implications for resurfacing and impactor populations, *Science, 329*(5998), 1504–7, doi:10.1126/science.1195050.

Helfenstein, P., and J. Veverka (1987), Photometric properties of lunar terrains derived from Hapke's equation, *Icarus, 72*(2), 342–357, doi:10.1016/0019-1035(87)90179-5.

Hendrix, A. R., and F. Vilas (2006), The effects of space weathering at UV wavelengths: S-class asteroids, *Astron. J.*, *132*(3), 1396–1404, doi:10.1086/506426.

Hendrix, A. R., et al. (2012), The lunar far-UV albedo: Indicator of hydration and weathering, *J. Geophys. Res.*, *117*, E12001, doi:10.1029/2012JE004252.

Hillier, J. (1999), Multispectral photometry of the Moon and absolute calibration of the Clementine UV/Vis camera, *Icarus, 141*(2), 205–225, doi:10.1006/icar.1999.6184.

Housley, R. M., R. W. Grant, and N. E. Paton (1973), Origin and characteristics of excess Fe metal in lunar glass welded aggregates, in *Proceedings of the Fourth Lunar Science Conference, (Supplement 4, Geochmica et Cosmochimica Acta)*, vol. 3, pp. 2737–2749.

Ingersoll, A. P., T. Svitek, and B. C. Murray (1992), Stability of polar frosts in spherical bowl-shaped craters on the Moon, Mercury, and Mars, *Icarus, 100*(1), 40–47, doi:10.1016/0019-1035(92)90016-Z.

Johnson, J. R., T. D. Swindle, and P. G. Lucey (1999), Estimated solar wind-implanted helium-3 distribution on the Moon, *Geophys. Res. Lett.*, *26*(3), 385–388, doi:10.1029/1998GL900305.

Kadish, S. J., C. I. Fassett, J. W. Head, D. E. Smith, M. T. Zuber, G. A. Neumann, and E. Mazarico (2011), A global catalog of large lunar craters (≥20 km) from the Lunar Orbiter Laser Altimeter, in *Lunar Plan. Sci. Conf., XLII*, abstract 1006., LPI Houston.

Keller, L. P., and S. J. Clemett (2001), Formation of nanophase iron in the lunar regolith, in *Lunar Plan. Sci. Conf., XXXII*, abstract 2097., LPI Houston.

Keller, L. P., and D. S. McKay (1993), Discovery of vapor deposits in the lunar regolith, *Science, 261*(5126), 1305–7, doi:10.1126/science.261.5126.1305.

Keller, L. P., and D. S. McKay (1997), The nature and origin of rims on lunar soil grains, *Geochim. Cosmochim. Acta, 61*(11), 2331–2341, doi:10.1016/S0016-7037(97)00085-9.

Kodama, S., et al. (2010), Characterization of multiband imager aboard SELENE, *Space Sci. Rev.*, *154*(1-4), 79–102, doi:10.1007/s11214-010-9661-z.

Lane, A. P., and W. M. Irvine (1973), Monochromatic phase curves and albedos for the lunar disk, *Astron. J.*, *78*, 267, doi:10.1086/111414.

Lucey, P. G., and M. A. Riner (2011), The optical effects of small iron particles that darken but do not redden: Evidence of intense space weathering on Mercury, *Icarus, 212*(2), 451–462, doi:10.1016/j.icarus.2011.01.022.

Lumme, K., and W. M. Irvine (1982), Radiative transfer in the surfaces of atmosphereless bodies. III—Interpretation of lunar photometry, *Astron. J.*, *87*, 1076, doi:10.1086/113192.

McGovern, J. A., D. B. Bussey, B. T. Greenhagen, D. A. Paige, J. T. S. Cahill, and P. D. Spudis (2013), Mapping and characterization of non-polar permanent shadows on the lunar surface, *Icarus*, *223*(1), 566–581, doi:10.1016/j.icarus.2012.10.018.

Mitrofanov, I., et al. (2010), Hydrogen mapping of the lunar south pole using the LRO neutron detector experiment LEND, *Science*, *330*(6003), 483–6, doi:10.1126/science.1185696.

Morris, R. V. (1980), Origins and size distribution of metallic iron particles in the lunar regolith, in *Proceedings of the Eleventh Lunar Science Conference, (Supplement 14, Geochmica et Cosmochimica Acta)*, vol. 2, pp. 1697–1712.

Neumann, G. A., et al. (2013), Bright and dark polar deposits on Mercury: Evidence for surface volatiles, *Science*, *339*(6117), 296–300, doi:10.1126/science.1229764.

Nozette, S., et al. (1994), The Clementine mission to the Moon: Scientific overview, *Science*, *266*(5192), 1835–9, doi:10.1126/science.266.5192.1835.

Nozette, S., C. L. Lichtenberg, P. Spudis, R. Bonner, W. Ort, E. Malaret, M. Robinson, and E. M. Shoemaker (1996), The Clementine Bistatic Radar Experiment, *Science*, *274*(5292), 1495–1498, doi:10.1126/science.274.5292.1495.

Ohtake, M., et al. (2010), Deriving the absolute reflectance of lunar surface using SELENE (Kaguya) multiband imager data, *Space Sci. Rev.*, *154*(1-4), 57–77, doi:10.1007/s11214-010-9689-0.

Ohtake, M., et al. (2013), One Moon, many measurements 3: Spectral reflectance, *Icarus*, *226*(1), 364–374, doi:10.1016/j.icarus.2013.05.010.

Paige, D. A., et al. (2010), Diviner Lunar Radiometer observations of cold traps in the Moon's south polar region, *Science*, *330*(6003), 479–82, doi:10.1126/science.1187726.

Pieters, C. M., et al. (2009), Character and spatial distribution of OH/H$_2$O on the surface of the Moon seen by M3 on Chandrayaan-1, *Science*, *326*(5952), 568–72, doi:10.1126/science.1178658.

Pieters, C. M., et al. (2013), One Moon, many measurements 1: Radiance values, *Icarus*, *226*(1), 951–963, doi:10.1016/j.icarus.2013.07.008.

Salvail, J. R., and F. P. Fanale (1994), Near-surface ice on Mercury and the Moon: A topographic thermal model, *Icarus*, *111*(2), 441–455, doi:10.1006/icar.1994.1155.

Shevchenko, V. V. (1982), The lunar photometric constant in the system of true full Moon, in *Sun and Planetary System*, vol. 96, edited by W. Fricke and G. Teleki, pp. 263–264, D. Reidel, Dordrecht.

Smith, D. E. (1999), The global topography of Mars and implications for surface evolution, *Science*, *284*(5419), 1495–1503, doi:10.1126/science.284.5419.1495.

Smith, D. E., et al. (2001), Mars Orbiter Laser Altimeter: Experiment summary after the first year of global mapping of Mars, *J. Geophys. Res.*, *106*(E10), 23,689–23,722, doi:10.1029/2000JE001364.

Smith, D. E., et al. (2010a), Initial observations from the Lunar Orbiter Laser Altimeter (LOLA), *Geophys. Res. Lett.*, *37*, L18204, doi:10.1029/2010GL043751.

Smith, D. E., et al. (2010b), The Lunar Orbiter Laser Altimeter Investigation on the Lunar Reconnaissance Orbiter Mission, *Space Sci. Rev.*, *150*(1-4), 209–241, doi:10.1007/s11214-009-9512-y.

Sudarsky, D., A. Burrows, and P. Pinto (2000), Albedo and reflection spectra of extrasolar giant planets, *Astrophys. J.*, *538*(2), 885–903, doi:10.1086/309160.

Sun, X., G. A. Neumann, J. B. Abshire, and M. T. Zuber (2006), Mars 1064 nm spectral radiance measurements determined from the receiver noise response of the Mars Orbiter Laser Altimeter, *Appl. Opt.*, *45*(17), 3960, doi:10.1364/AO.45.003960.

Sunshine, J. M., T. L. Farnham, L. M. Feaga, O. Groussin, F. Merlin, R. E. Milliken, and M. F. A'Hearn (2009), Temporal and spatial variability of lunar hydration as observed by the Deep Impact spacecraft, *Science*, *326*(5952), 565–8, doi:10.1126/science.1179788.

Urey, H. C. (1952), *The Planets: Their Origin and Development*, Yale Univ. Press, New Haven, Conn.

Vasavada, A. R. (1999), Near-surface temperatures on Mercury and the Moon and the stability of polar ice deposits, *Icarus*, *141*(2), 179–193, doi:10.1006/icar.1999.6175.

Verbiscer, A. J., D. E. Peterson, M. F. Skrutskie, M. Cushing, P. Helfenstein, M. J. Nelson, J. D. Smith, and J. C. Wilson (2006), Near-infrared spectra of the leading and trailing hemispheres of Enceladus, *Icarus*, *182*(1), 211–223, doi:10.1016/j.icarus.2005.12.008.

Warell, J. (2004), Properties of the Hermean regolith: IV. Photometric parameters of Mercury and the Moon contrasted with Hapke modelling, *Icarus*, *167*(2), 271–286, doi:10.1016/j.icarus.2003.10.010.

Warren, S. G., and R. E. Brandt (2008), Optical constants of ice from the ultraviolet to the microwave: A revised compilation, *J. Geophys. Res.*, *113*, D14220, doi:10.1029/2007JD009744.

Watson, K., B. C. Murray, and H. Brown (1961), The behavior of volatiles on the lunar surface, *J. Geophys. Res.*, *66*(9), 3033–3045, doi:10.1029/JZ066i009p03033.

Zuber, M. T., D. E. Smith, S. C. Solomon, D. O. Muhleman, J. W. Head, J. B. Garvin, J. B. Abshire, and J. L. Bufton (1992), The Mars Observer laser altimeter investigation, *J. Geophys. Res.*, *97*(E5), 7781–7797, doi:10.1029/92JE00341.

Zuber, M. T., et al. (2012), Constraints on the volatile distribution within Shackleton crater at the lunar south pole, *Nature*, *486*(7403), 378–81, doi:10.1038/nature11216.